A Study on Tensile Properties of Alloy 709, at various temperatures

Upadhayay, Swathi; Li, Hangyue; Bowen, Paul; Rabiei, Afsaneh

DOI:
10.1016/j.msea.2018.06.089

A Study on Tensile Properties of Alloy 709, at various temperatures

Swathi Upadhayay, Hangyue Li, Paul Bowen, Afsaneh Rabiei

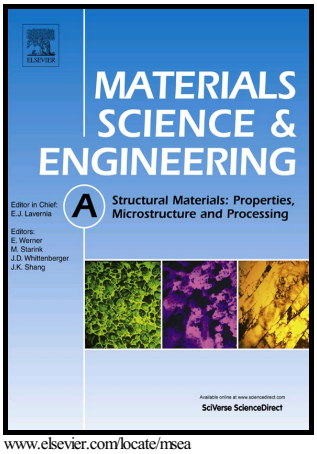

www.elsevier.com/locate/msea

PII: S0921-5093(18)30893-1
DOI: https://doi.org/10.1016/j.msea.2018.06.089
Reference: MSA36644

To appear in: *Materials Science & Engineering A*

Received date: 20 February 2018
Revised date: 14 May 2018
Accepted date: 22 June 2018

Cite this article as: Swathi Upadhayay, Hangyue Li, Paul Bowen and Afsaneh Rabiei, A Study on Tensile Properties of Alloy 709, at various temperatures, *Materials Science & Engineering A,* https://doi.org/10.1016/j.msea.2018.06.089

A Study on Tensile Properties of Alloy 709, at various temperatures

Swathi Upadhayay[1], Hangyue Li[2], Paul Bowen[2], Afsaneh Rabiei[1],

1. Advanced Materials Research Laboratory (AMRL), Department of Mechanical and Aerospace Engineering, North Carolina State University, Raleigh, NC – 27606, USA

2. School of Metallurgy and Materials, University of Birmingham, Edgbaston, Birmingham-B15 2TT, UK

*Corresponding author: Professor Afsaneh Rabiei
Email: arabiei@ncsu.edu

Declaration of Interest: none.

Abstract

In recent years, there have been several advancements in energy production from both fossil fuels and the alternate "clean" sources such as nuclear fission. These advancements are fueled by the need for more efficient systems that will optimize the use of the depleting fossil fuel reserves and shift the focus to cleaner sources of energy. The efficiency of any power generation cycle is dependent on the ability of the structural material to withstand the increased peak operating temperatures. Advanced austenitic stainless steels have been in the focus as structural material for the next generation nuclear power plants, due to their strength, corrosion resistance, weldability and the wide range of temperatures at which the austenitic phase is stable. Alloy 709, a recently developed advanced austenitic stainless steel, is being investigated in this paper. In

this study, tensile tests were conducted on dog-bone samples of Alloy 709 in an in-situ scanning electron microscope (SEM) loading and heating stage, equipped with electron backscatter diffraction (EBSD), at various temperatures. The in-situ experiments indicated that the material primarily accommodated deformation by slip at lower temperatures. Void formation and coalescence at grain boundaries preceded slip at higher temperatures. Although crack initiation at all elevated temperatures was intergranular, the crack propagation through the material and the final fracture was trangranular ductile. Additionally, tensile tests were conducted on larger cylindrical samples at 550, 650 and 750 °C in air. The results of tests conducted in air and in-situ were found to be in agreement, at these temperatures.

Keywords: Austenitic Stainless Steel, Alloy 709, Fractography, In-situ Scanning Electron Microscope, Electron Backscatter Diffraction.

1. Introduction

Structural materials used in the next generation nuclear power plants with improved efficiencies need to operate at high temperatures and withstand resultant extreme conditions. Therefore, superior mechanical strength, creep resistance and corrosion resistance are some of the desired properties in a candidate structural material. Advanced austenitic stainless steels are being investigated for these applications. Austenitic stainless steels are mostly Fe-C-Ni-Cr alloys, where the Cr is added for corrosion resistance and Ni is added to counteract the ferritic stabilizing nature of Cr and stabilize the austenite phase. Several austenitic stainless steels have been developed with variations in their chemistry and heat treatment to suit different

applications. These steels, specially the advanced austenitic stainless steels rely on secondary phases or precipitates for their characteristic strength and mechanical properties. Sourmail has reviewed the common precipitates observed in creep resistant austenitic stainless steel [1]. The 316H steel is a heat resistant, higher carbon variant of the 316 Stainless Steel (18Cr-12Ni austenitic stainless steel) and is often used to compare the performance of newer alloys. The precipitates observed in this alloy are mainly $M_{23}C_6$, a predominantly Cr rich carbide typically at grain boundaries, and intermetallics such as Fe_2Mo, FeCrMo and σ-phase [2]. Although, fine intermetallic Laves precipitate have shown to improve creep properties in an austenitic steel [3], after long aging times these precipitates coarsen at grain boundaries and triple points [2] reducing the creep strength of the alloy. High Temperature Ultrafine Precipitation Strengthened Steels (HT-UPS) developed by ORNL outperform the 316H steels in creep rupture life [3]. The strength of this 14Cr-16Ni austenitic stainless steel is attributed to the fine MC, M_6C, $M_{23}C_6$ and FeTiP precipitates that nucleate on dislocations. [3] Carroll studied the fatigue properties of the HT-UPS alloy and found that oxidation was a major problem in these alloys when compared to the 316H [4]. To improve corrosion resistance, advanced HT-UPS was developed with added Aluminum for corrosion resistance. The passive chromium oxide in conventional stainless steels are vulnerable in atmospheres containing water vapor [5]. Alumina forming austenitic steels, specifically the advanced HT-UPS with added Al, performed better in terms of oxidation resistance in water vapor environments, which was further enhanced with added Nb [5,6]. HT-UPS alloys with added Al and no Ti or V also performed better in terms of creep resistance when compared to other variants [7].

Alloy 709 is a 20Cr-25Ni advanced austenitic stainless steel developed as an improvement over the existing advanced austenitic stainless steels. The high Ni content provides increased austenite stability [8]. Sourmail et al. [9] have studied the effects of high temperature on the microstructure and secondary phases in the NF709 alloy. The NF709 alloy is a proprietary alloy of Nippon Steel & Sumimoto Steel, similar in composition to the Alloy 709 being studied in this paper. The NF709 alloy reported 0.05 wt.% Ti content while the Alloy 709 studied in this paper contains <0.01 wt.% Ti. The authors found coarse undissolved nitrides, carbides and carbonitrides such as $M_{23}C_6$ and (Nb,Ti)CN, in the NF709, after aging [9]. This precipitate evolution was also simulated by Shim et al [10]. NF709 possesses highest creep rupture strength amongst the austenitic steels. Preliminary studies performed indicated that Alloy 709 is superior to the HT-UPS alloys in tensile strength, thermal stability, creep-fatigue, sodium compatibility and weldability [8]. The excellent creep resistance and corrosion resistance of the Alloy 709 has made it the ideal candidate for next generation nuclear power plants.

In this study, in-situ scanning electron microscope (SEM) tensile tests were conducted on Alloy 709 to establish its yield and ultimate tensile stress at various temperatures from room temperature to 1000 °C. To characterize the behavior of the material and dominant deformation mechanisms at different temperatures and strain rates, electron backscatter diffraction (EBSD) was used to observe microstructural evolution and phase changes in the alloy.

2. Experimental Setup

A 400-pound ingot of Alloy 709 was fabricated using vacuum-induction melting (VIM) and electro-slag remelting (ESR) processes. 203 mm diameter round ingot from the VIM was homogenized at 1250°C for 4 hours. Half of this ingot was hot forged to a 203mm × 34.9 mm

bar at 1100°C. 1/3 of the hot-forged bar was rolled to 102mm × 20.3 mm at 1100°C. The hot-rolled bar was finally annealed at 1100°C for 2 hours, followed by water quenching. The composition of the alloy is shown in Table 1. Preliminary observations by the manufacturer indicated that the microstructure consists of uniform equiaxed grain structure with the ASTM GS# 4 to 6 (44 µm to 80 µm) Vickers hardness is found to be 176 ± 7.

Elements	**C**	**Mn**	**Si**	**P**	**S**	**Cr**	**Ni**	**Mo**	**N**	**Ti**	**Nb**	**B**	**Fe**
Composition wt%	**0.063**	**0.88**	**0.28**	**<0.005**	**<0.001**	**19.69**	**25.00**	**1.46**	**0.14**	**<0.01**	**0.23**	**0.0022**	**Balance**

Table 1. Composition of the as received alloy, post Electro Slag Remelting (ESR).

Tensile samples were extracted from the supplied plates with the longitudinal of the samples parallel to the rolling direction and the transverse directions respectively, using electro discharge machining (EDM). The dimensions of the samples designed for in-situ SEM experimentation had to adhere to the constraints imposed by the in-situ heating and loading stage (Kammrath & Weiss GmbH) and the ASTM E8 standards. The in-situ SEM setup is shown in Figure 1 and sample dimensions are shown in Figure 2.

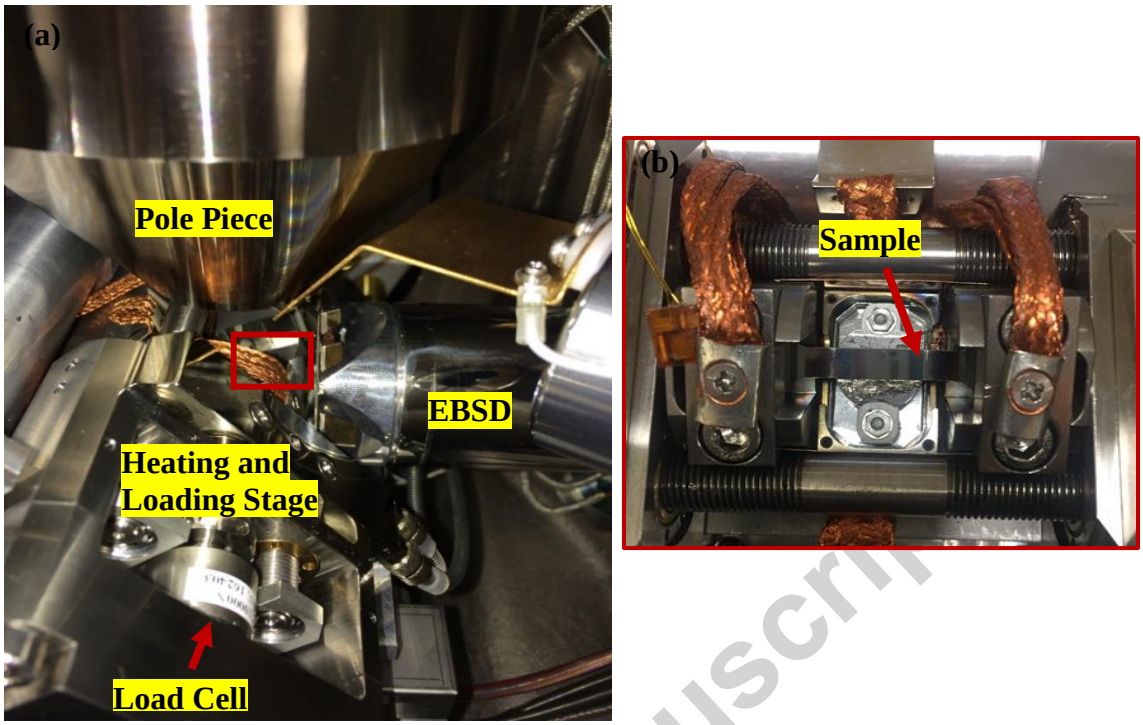

Figure 1.(a) Image of the In-situ SEM setup- (b) Sample clamped with the heater underneath.

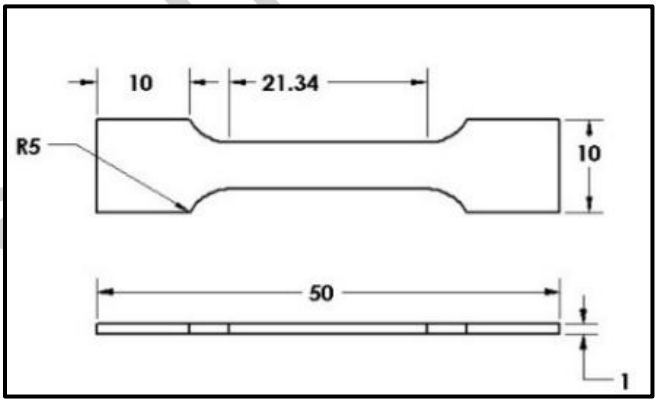

Figure 2. Dimensions (in mm) of the tensile sample.

Samples were ground beginning with 320 grit to 2400 grit, followed by ion-milling. To prevent any oxide formation at the surface of the sample during loading and heating to allow for EBSD after extended exposure at temperatures from 550 °C to 950 °C inside SEM chamber, the samples were sputter-coated with a thin (3.85 nm) layer of Au-Pd.

The in-situ SEM setup consists of Hitachi SU3500 scanning electron microscope, a Kammrath & Weiss GmbH heating and loading stage and Oxford Instruments Nordlys EBSD detector.

The heating and loading stage is mounted in the SEM vacuum chamber and can uniaxially load the sample while heating it. The stage is fitted with a load cell of maximum load specification of 10,000 N. Samples are loaded by the means of the leadscrews. The front and the rear yoke move along the leadscrew simultaneously upon loading, ensuring both sides of the samples are loaded equally to prevent shifting of the viewed region during in-situ testing. Elongation of the sample is measured using a linear variable differential transformer (LVDT) and the output is recorded live and displayed on the DDS32 software. The 140 mm diameter ceramic heater plate is located right underneath the tensile specimen that can be controlled via the heater controller either manually or via the DDS software. This heater can heat the sample to a maximum temperature of 300 °C under atmospheric pressure and a maximum temperature of 1000 °C under vacuum. Sample temperature is monitored by a thermocouple placed right under the sample. The displacement rate of the loading can be adjusted on the motor control settings in the DDS software and can range from 0.1 μm/s to 20 μm/s. The loading is interrupted at certain intervals by turning the motor off, while capturing SEM images or performing EBSD mapping.

To ensure the safety of the critical components on stage and within the SEM chamber, the temperatures at various points are monitored using additional thermocouples and kept within acceptable temperature limits by a cooling system.

Energy dispersive X-ray spectrometer (EDS) on a FEI Verios 460L field-emission scanning electron microscope (FESEM) was used on polished samples to identify the precipitates

and phases in Alloy 709 samples. The in- situ SEM uniaxial tensile tests were performed at room temperature, 550, 650, 750, 850 and 950 °C. All samples were tested along the rolling direction, except 4 samples tested at 750 °C – 2 of which were loaded along the rolling direction and 2 along the transverse direction. During in-situ SEM loading, sample was heated at the rate of 25 K/min, first to 100 °C and then to the target temperature of 550, 650, 750, 850 or 950 °C. Before heating is begun, the sample loaded to a constant preload of 25 N, to ensure only tensile loads on the sample. All the tensile tests were performed at the strain rate of 5.02×10^{-3} /min as per ASTM E21 standard for tensile tests at elevated temperature. One tensile test was performed at a strain rate of 2.61×10^{-4} /min to study the effect of strain rate. Note that fractography was performed on selected samples to assist the interpretation of deformation mechanisms.

The test matrix is presented in Table 2. During the test, in addition to SEM images, EBSD mapping was performed to observe changes in microstructure. The results obtained from these small tensile specimens were compared with results obtained from standard tensile tests, conducted at temperatures of 550, 650 and 750 °C in air. Cylindrical testpieces were utilized here which contain a 25.3 mm long gauge section of 5 mm in diameter, and they were machined with the longitudinal of the testpiece parallel to the rolling direction. The testpiece geometry adopted has two shoulders which allow a high temperature extensometer to be attached to measure the extension of the gauge section during testing. The tests were conducted under cross-head displacement control with a ramp rate of 6×10^{-3} /min. Note that the resultant strain rate is similar to the ramp rate of the crosshead, but it can be slightly smaller especially on the elastic deformation regime. The testpieces were pulled to failure in all cases.

Table 2. Test matrix of tensile experiments

Temperature	Orientation	Strain Rate
25°C	RD	5.02×10^{-3} /min
550 °C	RD	5.02×10^{-3} /min
650 °C	RD	5.02×10^{-3} /min
750 °C	RD	5.02×10^{-3} /min
750 °C	TD	5.02×10^{-3} /min
800 °C	RD	2.61×10^{-4} /min
850 °C	RD	5.02×10^{-3} /min
950 °C	RD	5.02×10^{-3} /min

3. Results

3.1. Microstructural Characterization

The microstructural observation showed that the alloy comprises of an austenitic matrix with equiaxed grains of an average size between 48-50 μm (Figure 3(a)). Room temperature SEM observations show some large clusters of inclusions along the rolling direction plus some isolated transgranular precipitates. EDS analysis was performed at room temperature to establish the composition of the precipitates. The compositions of the matrix and different precipitates are shown in Figure 3. Majority of the precipitates were found to be Nb rich with traces of other elements like Mo, Ti and B. The precipitates that formed the oriented clusters (Figure 3(b)) were (5- 10 μm) in size while the isolated precipitates (Figure 3(c)) were ~ 5 μm in size. Much smaller, spheroidal Nb rich precipitations uniformly distributed through the matrix were also observed (Figure 3(c) Circled region). Only SEM scale precipitates were identified therefore, Z-phase and sigma phase ae not discussed in this paper. Additional analysis will be needed to account for the effects of these smaller precipitates. At higher temperatures, grain boundary $M_{23}C_6$ precipitation and precipitation within the grains becomes apparent. This is discussed later.

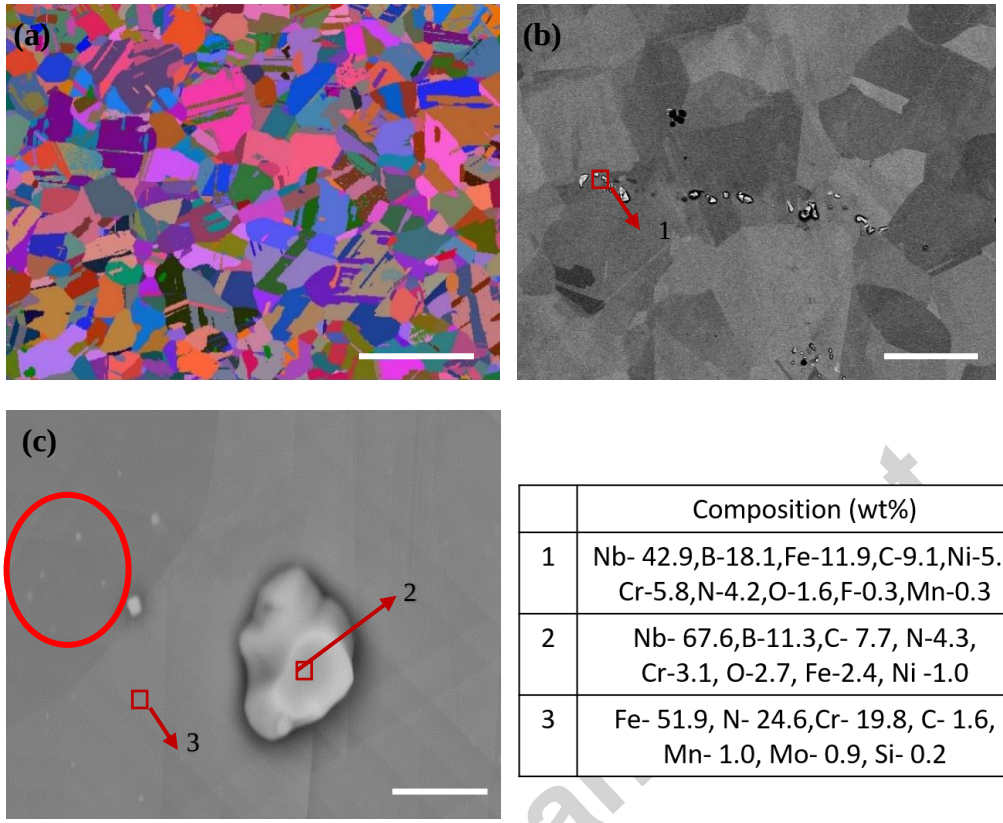

	Composition (wt%)
1	Nb- 42.9,B-18.1,Fe-11.9,C-9.1,Ni-5.9 Cr-5.8,N-4.2,O-1.6,F-0.3,Mn-0.3
2	Nb- 67.6,B-11.3,C- 7.7, N-4.3, Cr-3.1, O-2.7, Fe-2.4, Ni -1.0
3	Fe- 51.9, N- 24.6,Cr- 19.8, C- 1.6, Mn- 1.0, Mo- 0.9, Si- 0.2

Figure 3. A. EBSD Euler maps showing microstructure of as polished samples. B. Room temperature SEM with Backscatter Electron(BSE) image of clusters of Nb rich precipitates along Rolling Direction (RD). C. Isolated Nb rich precipitates. Table showing the compositions generated by EDS. ***Circled****-nanoscale Nb-rich precipitates.*

3.2. Tensile Experiments

3.2.1. Tensile Properties.

In-situ SEM tensile tests were performed at a constant strain rate of 5.02×10^{-3} /min at 25 °C, 550 °C, 650 °C, 750 °C, 850 °C and 950 °C. The macro images of the test-pieces under tension at high temperatures is shown in Figure 4. The test pieces all show uniform deformation and fail close to the centre of the reduce section.

The engineering stress-strain curves are shown in Figure 5(a) and (c) . The elastic region of the curves is elaborated in Figure 5(b). The drops in the curves corresponds to instances the tests

were interrupted for SEM imaging or EBSD mapping. The results of the experiments conducted have been tabulated in Table 3.

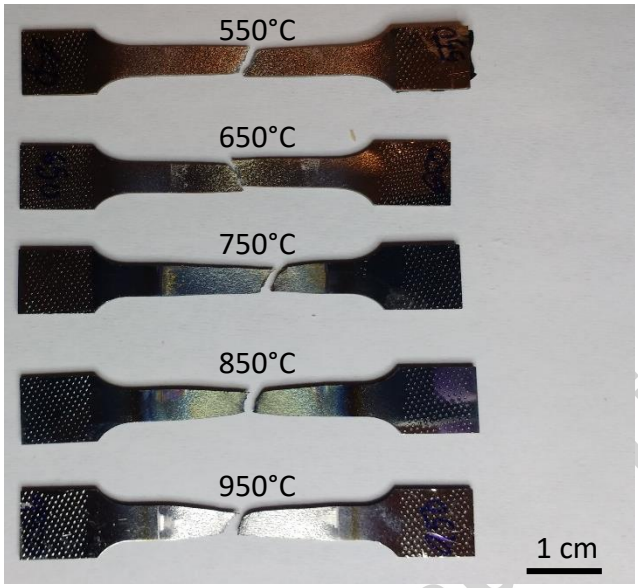

Figure 4. Test-pieces under tension at 550, 650, 750, 850 and 950°C.

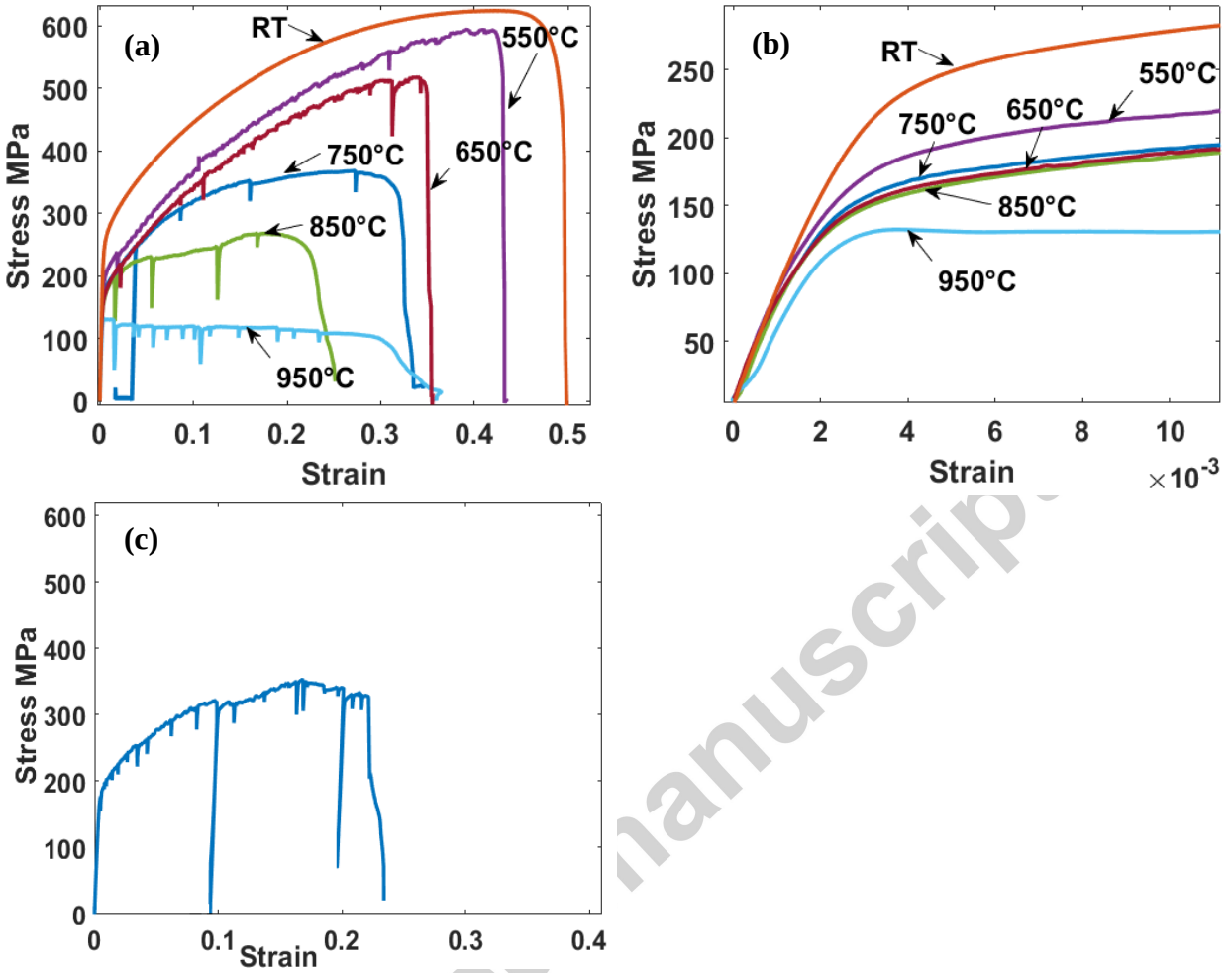

Figure 5. (a) Engineering stress-strain curve of Alloy 709 under tension at 25°C-950°C along RD. (b) Zoom in of the elastic region of the same. (c) Engineering stress-strain curve of sample at 800° at 2.61×10^{-4} /min strain rate.

Table 3. Tensile Properties of the Alloy 709 at various temperature along Rolling Direction (RD).

Temperature (°C)	Orientation	$\sigma_{0.2}$ (MPa)	Ultimate Tensile Strength (MPa)	Maximum Strain
25	RD	251	624	51%
550	RD	227	594	44%
650	RD	168	519	36%
750	RD	174	368	32%
850	RD	160	269	27%
950	RD	132	132	32%

It is observed that the modulus of elasticity varies slightly at different temperatures (Figure 5(b)). However, there is a major decrease in the yield stress of the material from room temperature to 950˚C, with the yield Stress at 650 °C being an outlier to the general trend over the various temperatures. At lower temperatures (RT, 550 and 650 °C), the material experiences work hardening. This phenomenon is due to the increased density of dislocations and is represented in the form of the gradual increase in the stress between yield strength and ultimate strength. At 550 and 650 °C thermal softening due to dislocation mobility comes into play but is dominated by the work hardening. At higher temperatures (≥ 750 °C), the thermal softening due to increased mobility of dislocations is able to cancel the effects of work hardening resulting in a decrease in the ultimate strength. The Engineering Stress-Strain curve of the sample at 950 °C shows that the sample reaches a maximum stress of 132 MPa at yield. The plastic region, at this temperature, is represented by a plateau or a very gradual drop. This decrease is because work hardening is completely dominated by thermal softening.

The engineering stress-strain curve of the tensile test conducted at a constant strain rate of 2.61×10^{-4} /min at 800 °C is shown in Figure 5(c). This strain rate provides extended exposure to high temperature.

Table 4. Tensile properties of Alloy 709 at 750 °C along rolling (RD) and transverse direction(TD).

Temperature (°C)	Orientation	Pre-crack	$\sigma_{0.2}$ (MPa)	Ultimate Tensile Strength (MPa)	Maximum Strain
750	RD	No	174	368	32%
750	TD	No	138	327	27%

At 750 °C, further experiments were conducted to understand the effect of rolling direction on the mechanical properties of the material (Figure 6(a) and (b)). The samples along transverse rolling direction show only a slight decrease in yield stress and maximum elongation.

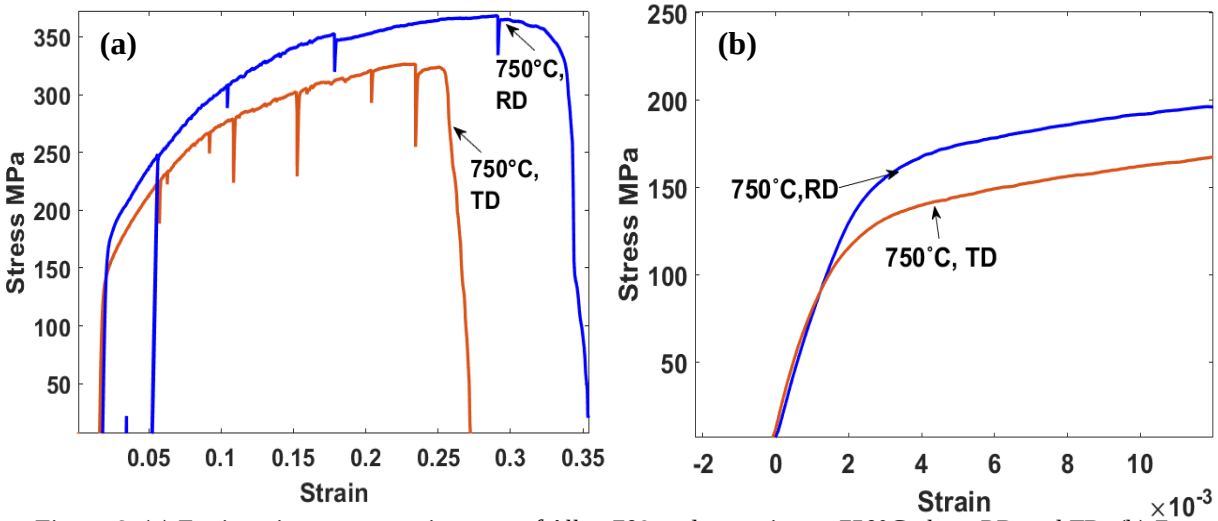

Figure 6. (a) Engineering stress-strain curve of Alloy 709 under tension at 750°C along RD and TD. (b) Zoom in of the elastic region of the same.

Serrations were observed in the plastic region of the tensile stress-strain graphs of Alloy 709 (Figure 7 and Figure 8). These are characteristics of dynamic strain aging and an indication of the work hardening as a result of interaction between solute atoms and mobile dislocations. In samples tested at 550˚C and 650 °C (Figure 7), the serrations are more prominent due to the dominating work hardening. Rodriguez [11] classified such serrations into 5 types – Type A, B , C, D and E. The serrations observed in Alloy 709 samples at 550, 650 are a combination of Type A and Type B, and a combination of Type A and Type C at 750 and 800 °C. In austenitic stainless steels, the serrations are due to the interaction of the mobile dislocation with solute atoms such as C, N, as indicated by the type B serrations, and diffusion of Ni and Cr in the alloy [12,13] at higher temperatures as indicated by Type C serrations. Previous work on 316LN, a low carbon, nitrogen enhanced austenitic stainless steel, has shown similar serration types [14–

16]. The serrations were observed in samples tested along both the rolling direction and transverse direction.

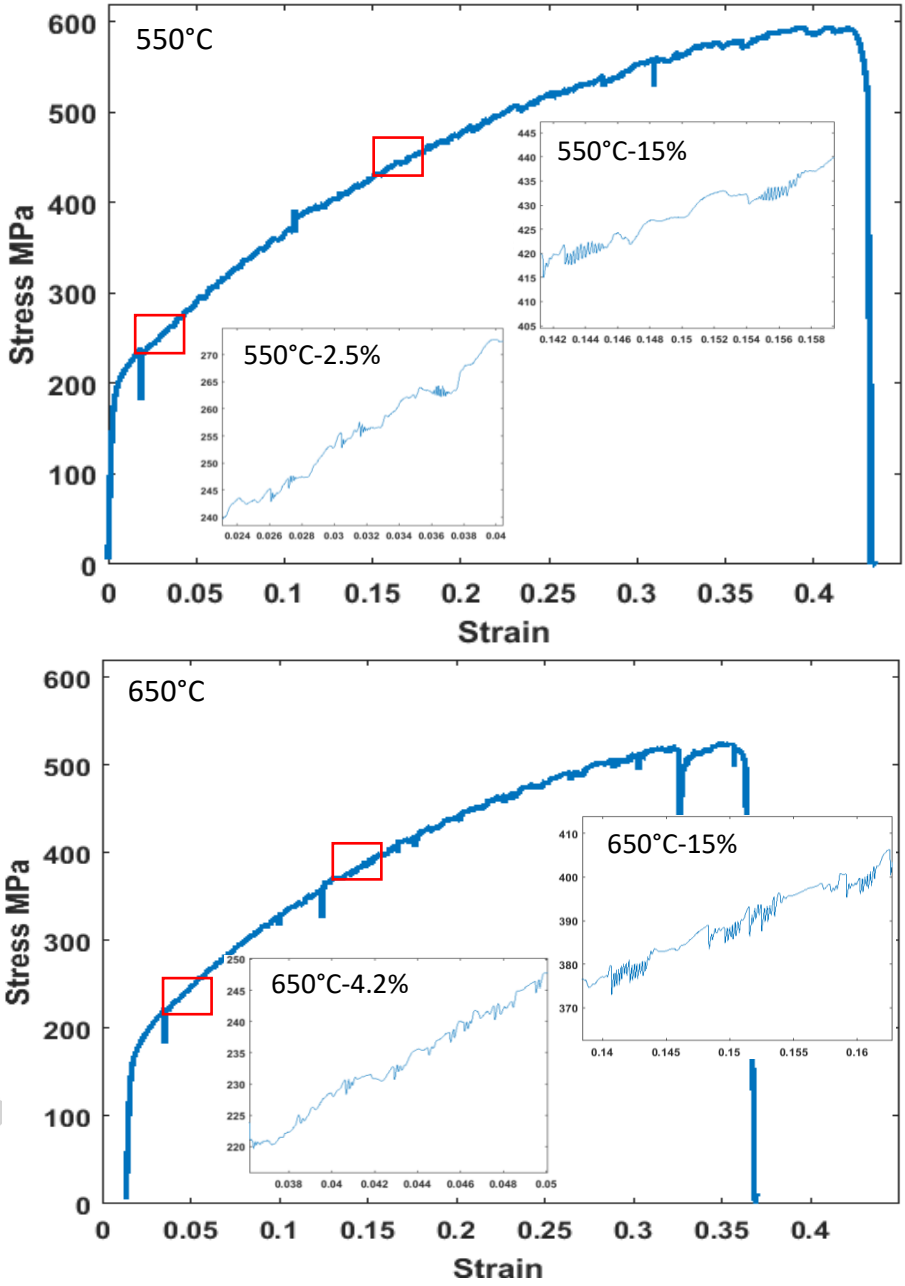

Figure 7. Type A and Type B serrations at 550°C ,650°C. Insets showing a zoom in of the engineering stress-strain curve at different strains.

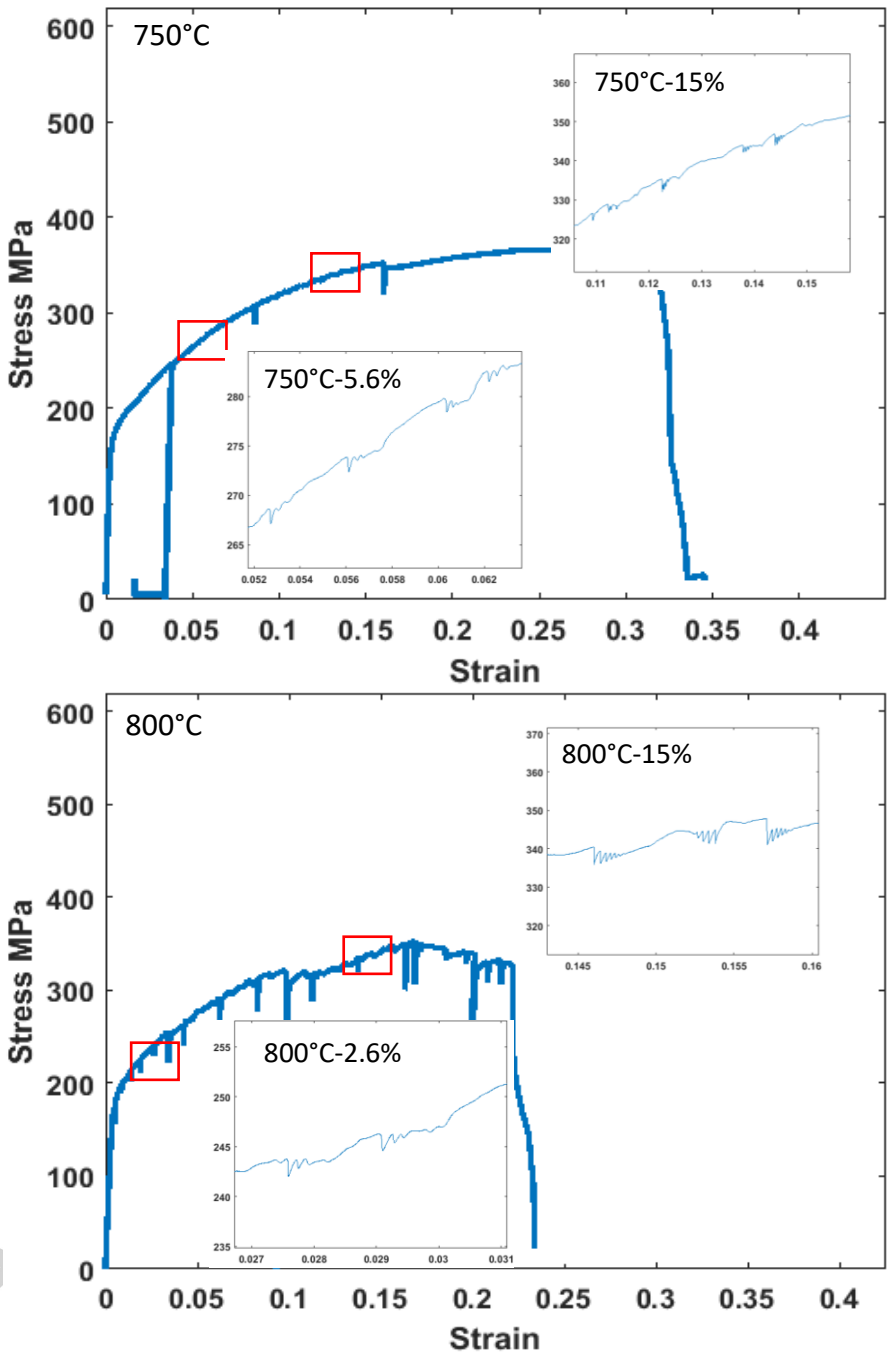

Figure 8. Type A and Type C serrations 750 °C at 5.021×10^{-3} /min and at 800 °C at 2.608×10^{-4} /min. Insets showing a zoom in of the engineering stress-strain curve at different strains.

Although precipitate growth occurs in austenitic steels at temperatures greater than 600 °C, serrations are evident at 650 °C, indicating that there are free solute atoms interacting with

the mobile dislocations. This interaction also contributes to the work hardening observed at 550 and 650 °C. The duration of the serrated period shortened with an increase in temperature. At 550 °C and 650 °C, the serrations are observed from the critical strain till failure, while at 750 °C, they disappear at 15% strain. Mannan et al[12], concluded that serrations can be correlated to the precipitation activity in the material. At higher temperatures, there is a decrease in the availability of free solute atoms due to significant precipitation growth, as observed in the sample tested at 950 °C, resulting in decrease in the serrations and their eventual disappearance. Growth of carbide precipitates deplete the interstitial solute atom carbon from the alloy, preventing interaction between solute atoms and mobile dislocations [12]. This results in the serrations being further apart and in reduced intensity of Type B serrations, and eventually in serrations disappearing as in the case of 750 °C after 15% strain. At 850 and 950 °C, no serrations were observed.

4. Discussion

550 and 650 °C:

In-situ SEM images of the sample surface provide insights into deformation regimes in the sample, the nature of crack propagation and changes in grain morphology. The behaviour of the alloy at room temperature and 550 °C are closely similar. At 550 °C and 650 °C, the plastic deformation is primarily accommodated via the formation of slip bands at all strain levels (Figure 9(a) & (b)). By increasing strains, the density of the slip bands increases, and multiple slip systems are observed in some grains. Elongation and slight rotation in larger grains is observed in the EBSD inverse pole figure (IPF) maps at 550 °C (Figure 9(c), (d) & (e)). Colour

gradation in the IPF plots indicates misorientation. In the samples tested at 550 °C, there is significant colour gradation especially in the larger grains. This is also an indication of slip bands in the grain, since constrained slip bands result in such misorientation. In addition to slip, creep mechanisms such as intergranular void nucleation and coalescence are observed in the samples tested at 550 and 650 °C, observed at 17.8% strain and 10.9% strain respectively. Since the interrupted tensile tests take 4-5 hours, some degree of creep interaction can be expected at elevated temperatures.

Intergranular crack initiation sites were observed in the edges of the sample, in all tensile tests at temperatures greater than 550 °C. At 550 °C, these cracks were first observed at 31% strain. These crack initiation sites convert into transgranular cracks which propagate through the width of the sample till they reach the intergranular sites on the other edge. At the interface of the intergranular and transgranular region, slip bands are observed (Figure 9(f) & (g)). Fractography shows that the nature of the fracture is transgranular ductile, with dimples of varying sizes (Figure 9(h) & (i)). This is observed in samples at 550 and 650 °C. The network of fine dimples is due to particle decohesion around the small Nb precipitates, and larger ones around the larger Nb rich carbides and carbonitrides. There are voids in the fracture surface, which indicates the creep void nucleation and growth at grain boundaries and around precipitates. The voids are more prominent at 650 °C due to greater extent of creep interaction (Figure 9(i)).

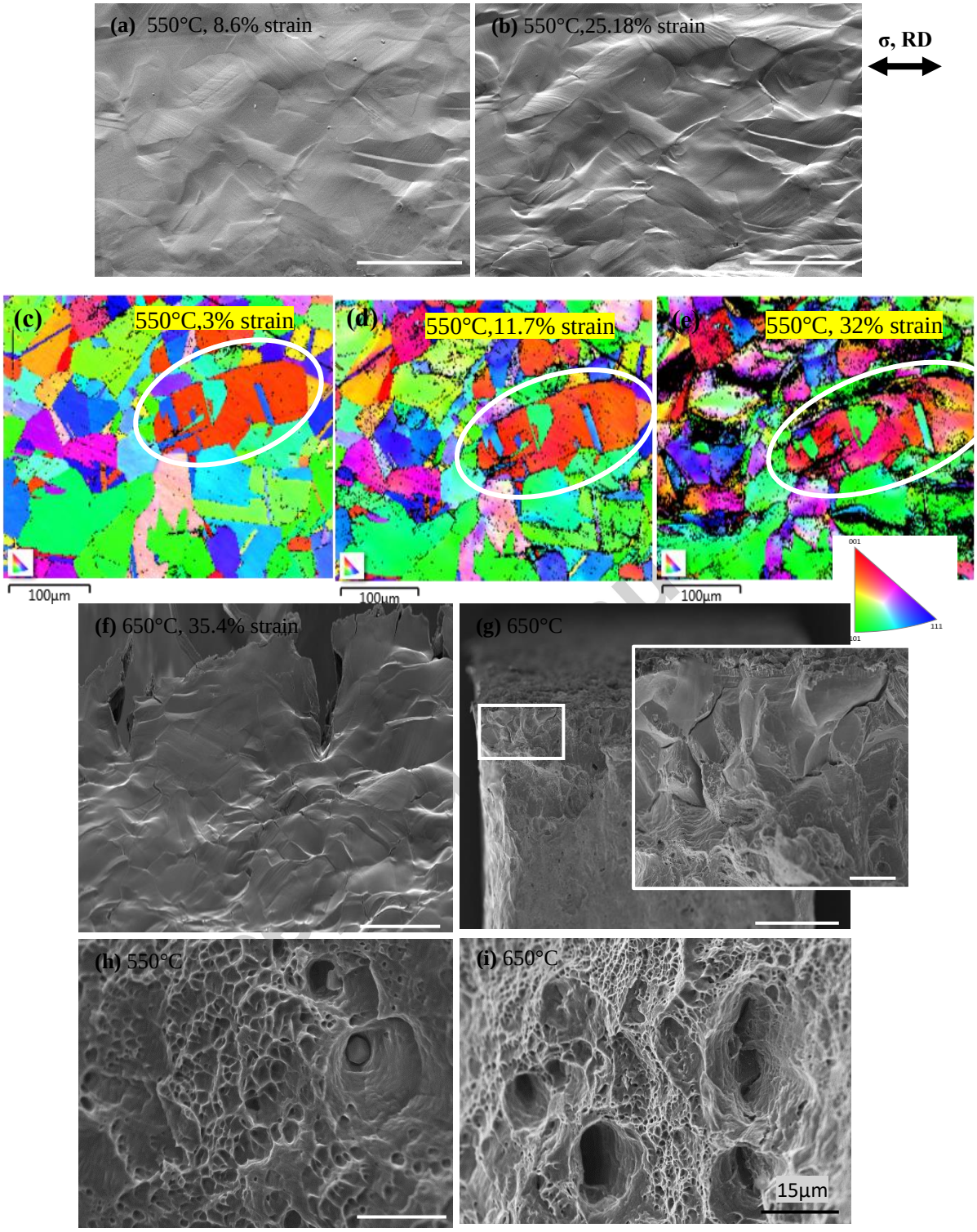

Figure 9.(a) and (b) Surface of sample at 550 °C showing slip bands at 8.6 and 25% strain (c), (d) and (e). IPF maps (parallel to ND) showing elongation and color gradation within grains (circled region) with increasing strain. (f) Intergranular crack initiation (at 35.4% strain) and (g) Corresponding region in the fracture surface. (h) and (i) Dimpled fracture surface of sample under tensile at 550 °Cand 650 °C.

750 °C:

At 750 ˚C and above, there is a shift in the deformation mechanism. The void formation and coalescence, observed beginning at 9% strain, precede the activation of the slip bands (Figure 10(a)&(b)). The voids are formed due to creep interaction. It was observed that the sample along transverse rolling direction exhibited similar deformation mechanism as the ones along rolling direction and showed shift from void formation and coalescence at lower strains to slip band activation at higher strains.

The fractographic images of the sample tested at 750 °C along the rolling direction are shown in Figure 10(c). The fracture surface features a network of smaller and larger dimples with inclusions at the bottom, similar to sample at 550 °C and 650 °C. At higher temperatures as the thermal softening begins to counteract the work hardening and precipitates coarsen, larger dimples are observed. In samples along transverse rolling direction, the effect of the oriented clusters of precipitates can be seen (Figure 10(d)). The dimples around these clusters is relatively shallow. This indicates that the crack growth is accelerated upon contact with these clusters, with reduced plasticity.

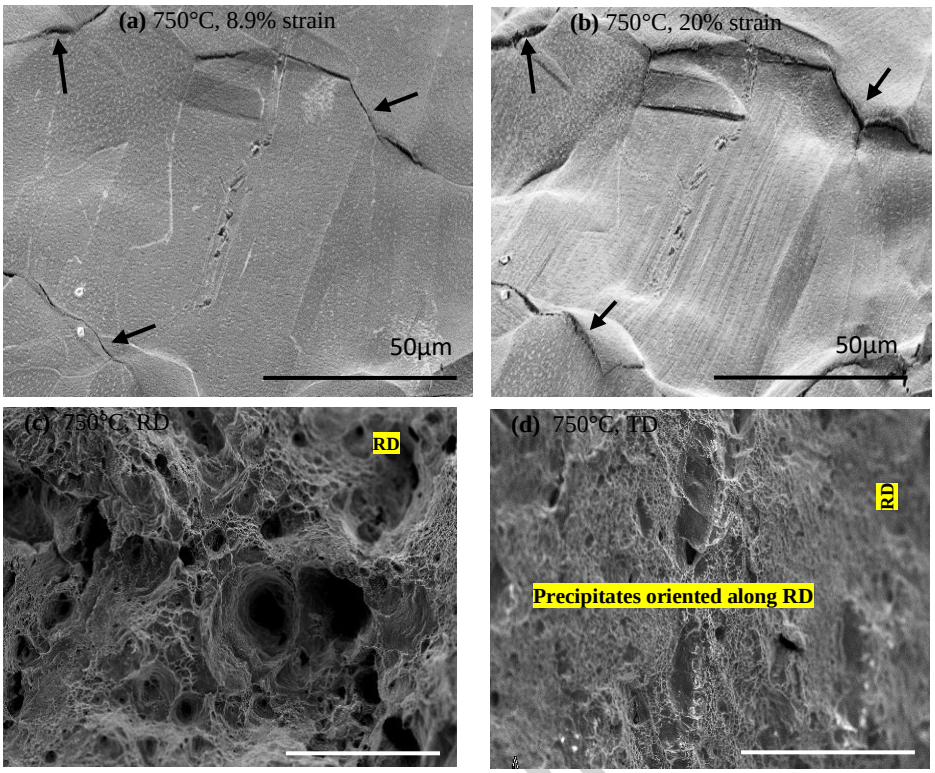

Figure 10. (a) & (b). Surface of sample at 750 °C at 8.9% and 20% strain showing a shift from void nucleation and coalescence to slip bands. (c) and (d): fractographic images of the samples along rolling and transverse direction.

850 °C and 950 °C:

At 850 °C in addition to the surface features observed at 750 °C, there were small cracks originating near the grain boundaries growing in to the grain (Figure 11 (a)). This can be due to debonding around nanoscale, needle shaped precipitates at grain boundaries growing into the grains. These cracks were observed throughout the surface of the sample but did not appear to grow significantly across the grains or alter the fracture path. Intergranular crack initiation sites and transgranular propagation to failure was observed, similar to samples tested at lower temperatures.

Due to a large amount of thermal softening and necking at 850 °C and 950 °C, the sample shows a narrow fracture surface indicating a major reduction in cross-section (Figure 11(e) &

(f)). There is still ample ductility at 850 °C in the samples as indicated by the presence of the dimples. On the surface, the creep-like void formation and coalescence was dominant until the onset of slip bands, and eventual failure. The numerous large voids on the fracture surface corroborate the surface observations. Grain boundary cracks were observed to grow more transverse to loading directions and these are the elongated voids seen in Figure 11(e).

Crack initiation at 950 °C was also intergranular at the edges. As the crack propagates, it is observed that the material around the crack begins to lose its crystallinity (Figure 11(b)). This loss of crystallinity is observed on the fractured surface and occurs due to a combination of the high temperature and stress around the crack.

In-situ SEM setup allowed EBSD mapping at temperatures up to 950 °C. The IPF maps along normal direction show that there is no significant elongation in the grains up to 4% strain (Figure 11(c)&(d)). There is also a lack of colour gradation within these grains, corresponding to the delayed activation of slip bands in samples tested at higher temperatures. Precipitation growth was observed on the surface of the sample at this temperature.

At 950 °C, dimples as observed at lower temperatures are not seen anymore. The fracture surface is incredibly narrow and features very large voids, some as large as 100 µm (Figure 11(f)). These voids appear like large cavities with pulled edges due to the great extent of thermal softening at the temperature.

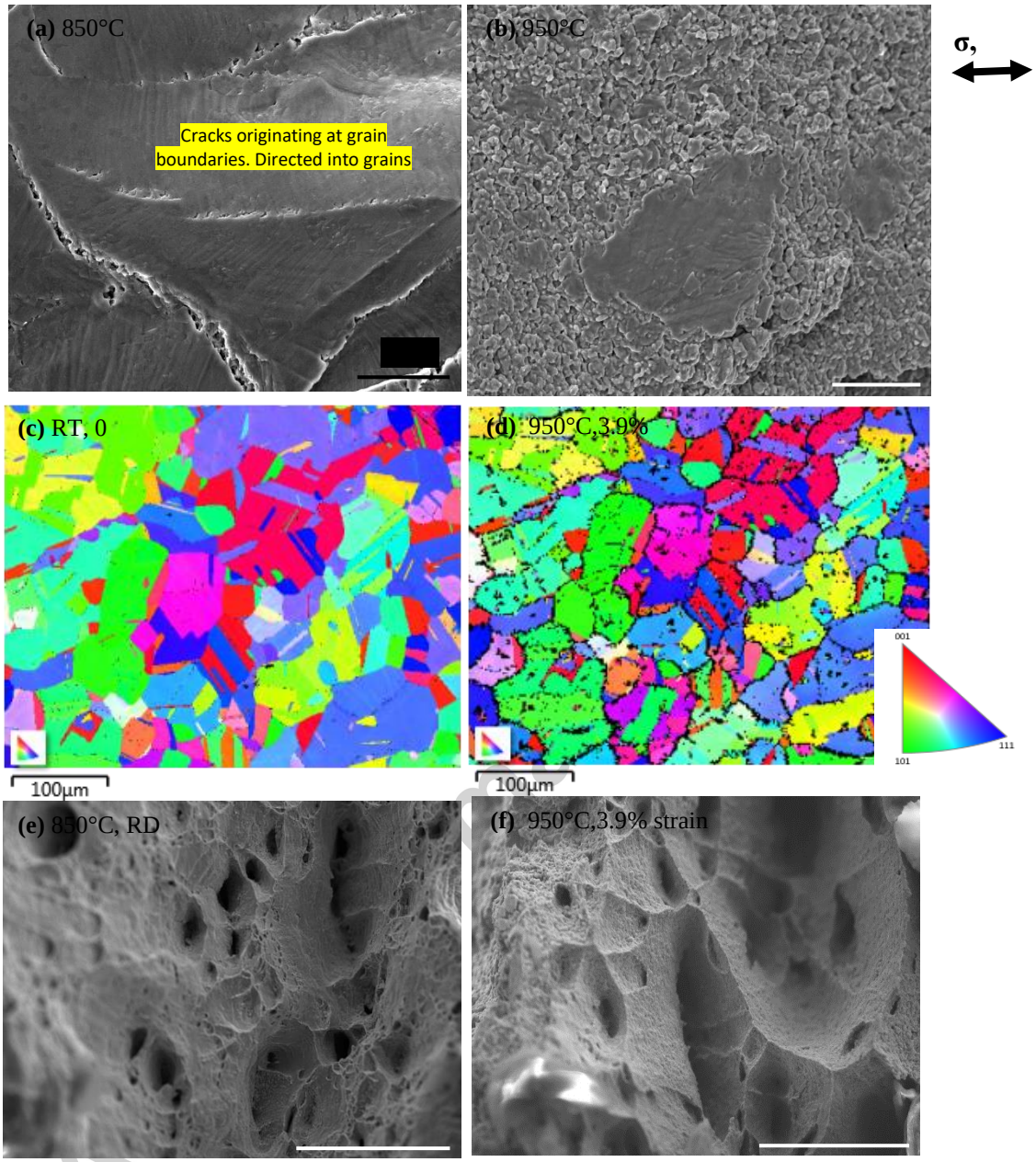

Figure 11. (a). In-situ SEM images of sample under tensile at 850 °C – showing cracks growing into grain boundary into the grains; and (b) 950 °C-showing loss of crystallinity around the crack propagation. (c) & (d): IPF (parallel to normal direction) of Alloy 709 sample at 950 °C. (e) & (f): Fractographic images of samples at 850 and 950 °C.

Grain boundary $M_{23}C_6$ precipitates, Nb rich precipitates within the grains were seen very prominently on the surface Figure 12(a). Some extent of debonding at the precipitate-matrix was observed (Figure 12(b)) but did not appear to grow significantly before sample failure. Phase changes in the Alloy 709 during heating and loading are also observed using in-situ SEM and

EBSD. There is an increase in BCC ferrite content at elevated temperatures, as shown in Table 5. The increase in the BCC ferrite is significantly larger at 950 °C when compared to 650 °C, even at lower strains. Such ferrite formation at the grain boundaries have been observed in 316H, and were found to be associated with creep cavitation. [19]

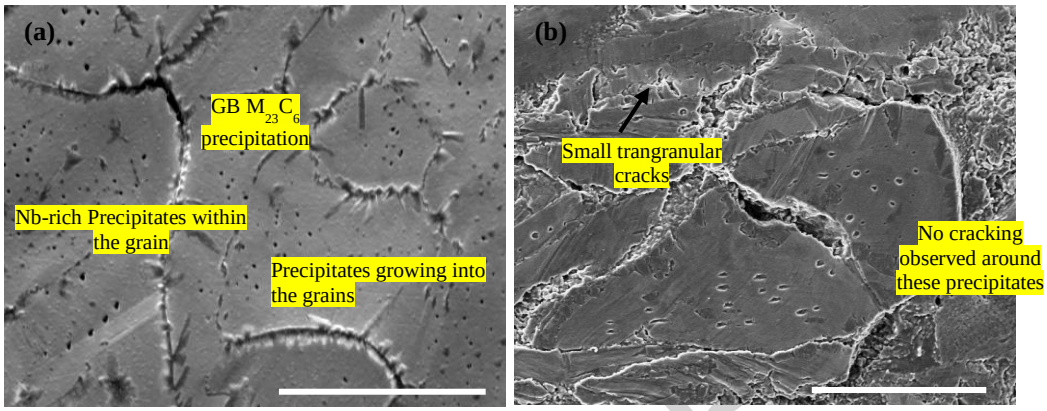

Figure 12. Grain boundary and transgranular precipitation growth observed in Alloy 709 sample under tension at 950°C.

Table 5. Increase in BCC iron content due to temperature and loading.

Temperature/Strain	0% (at 25°C)	3.9% strain	12.1% strain
650 °C	0.15% Fe-BCC	-	0.32% Fe-BCC
950 °C	0.15% Fe-BCC	2.25% Fe-BCC	-

800 °C at 2.61×10^{-4} /min :

Due to the slow loading rate and consequent longer exposure to the temperature, significant creep interaction can be expected. The surface deformation is like that observed at 750 °C and 850 °C, with greater macrocrack growth and grain boundary separation than that in the faster strain rate tensile experiments (Figure 13(a) & (b)). Series of SEM images of the same region, through increasing strains, were processed using MATLAB and binarized. These binarized images (Figure 14) emphasize the micro and macro cracks at grain boundaries, concentration of plastic deformation and eventual grain boundary separation at higher strains. At

lower strain there is grain boundary void formation and increasing strains these voids begin to grow (Figure 14(a)). At 15 and 18.9% strain, we see that these grain boundaries begin to separate plastically (Figure 14(c)). Figure 13(c) also shows the grain boundary cracks separating plastically ahead of the final transgranular crack propagation.

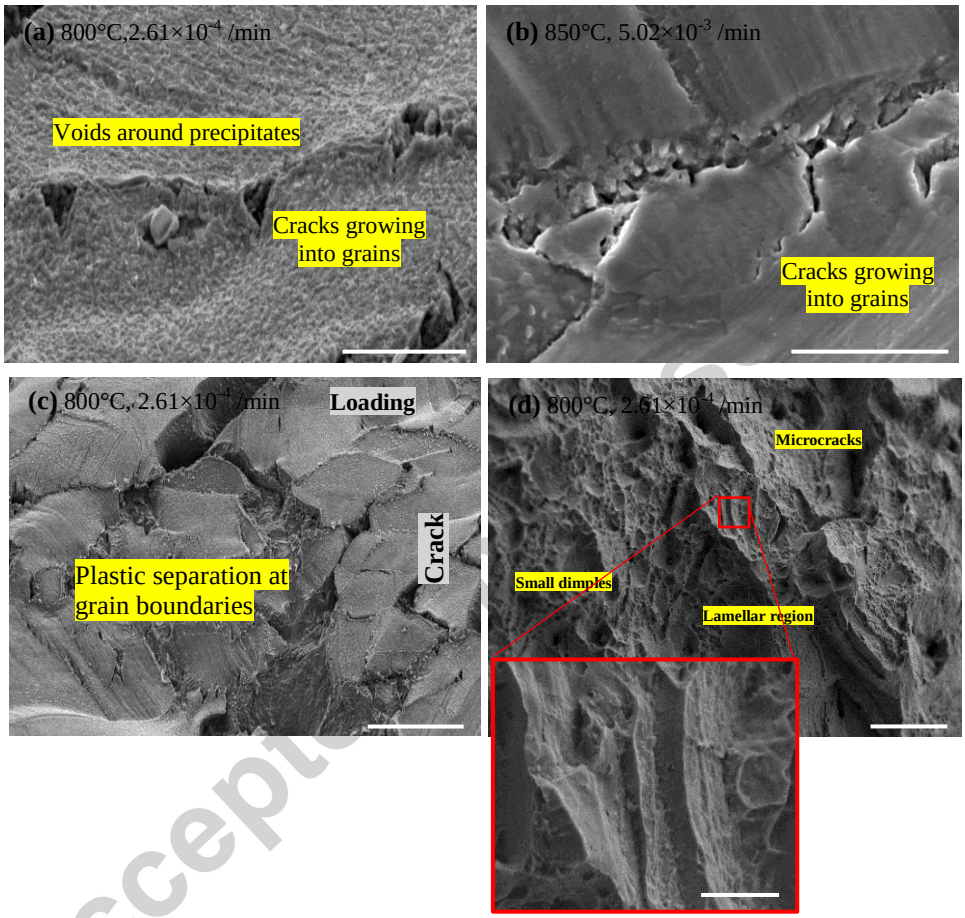

Figure 13. (a) & (b): SEM images comparing cracks growing from grain boundary into grains at 800°C (2.61×10^{-4} /min) and 850°C (5.02×10^{-3} /min). (c) Plastic separation of grain boundaries ahead of the crack tip. (d) Fracture surface of the sample.

The fracture surface of the sample under 2.61×10^{-4} /min tensile loading at 800 °C shows similar features as discussed previously. Along the direction of crack propagation, after the intergranular crack initiation region, an area of small but shallow dimples is observed indicating that at low strain creep mechanisms are dominant. Towards the end of the crack propagation, the

mode changes to lamellar/step like regions accompanied by dimples (Figure 13D- inset). A closer look at the lamellar region reveals alternating modes of transgranular region with microdimples and fast transgranular fracture.

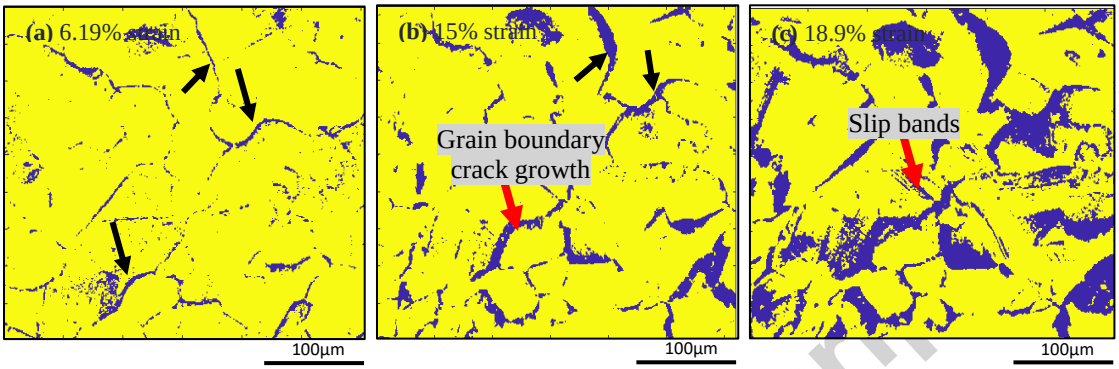

Figure 14. SEM images binarized using MATLAB highlighting grain boundary void nucleation and coalescence leading to cracking and plastic separation (c) at 800°C, 2.61×10^{-4} /min .

A summary of the crack initiation, propagation and final fracture observed for the lower temperatures (550-650 °C) and higher temperatures (750-950 °C) has been shown in Figure 15.

Comparison between in-situ SEM tensile tests and conventional tensile tests:

The results of tensile tests conducted in air are presented in Table 6. Despite differences in environment (vacuum vs. air), testpiece geometry (thin strip vs. cylindrical), limitation of heating area (local vs global), all tensile properties including yield stress, intimate tensile strength and elongation measured from in-situ SEM tests are closely similar to those that tested in the conventional way, which also demonstrate the same trend with respect of temperature dependence. Although in-situ SEM experiments tested a smaller volume of material, both sample geometries have a significant number of grains within the gauge sections, hence lead to similar properties. It is also observed that environment has little influence on deformation mechanisms in Alloy 709, which is dominated by microvoids coalescence. Fractographs of cylindrical sample tested at 750°C is shown in Figure 16.

	Low Temperature- 5.02×10^{-3} /min		High Temperature – 5.02×10^{-3} /min	
Crack Initiation	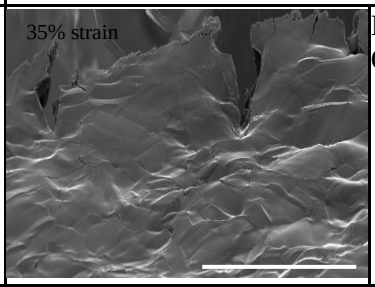	Intergranular Crack Initiation	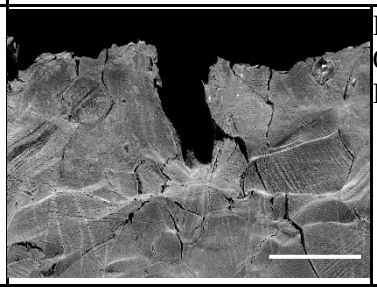	Intergranular Crack Initiation
Crack Propagation	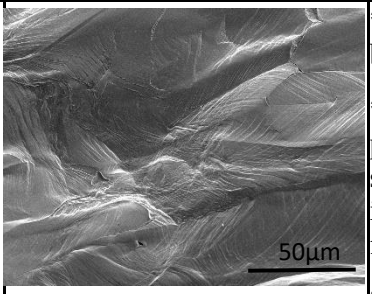	*Deformation by slip bands. *Crack propagates as slip bands interact and form a tangle. *Few intergranular void nucleation is also seen(arrows)	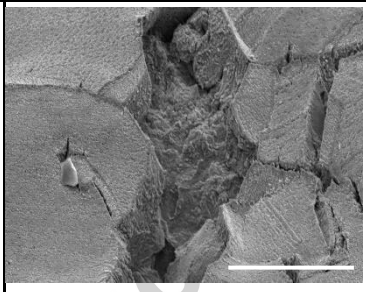	*Void nucleation and coalescence observed first. *Intergranular cracks are formed. *At higher strains, intergranular cracks separate plastically leading to transgranular propagation
Final Fracture	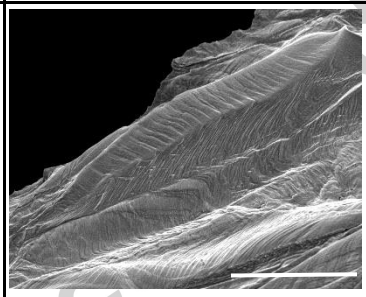	*Transgranular crack propagation with severe plastic deformation, as evident by the slip bands.	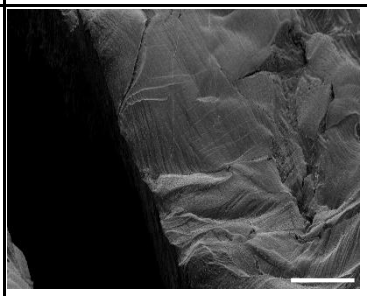	Transgranular crack propagation with plastic separation at the grain boundary cracks.

Figure 15. Summary of the In-situ SEM tensile experiments. Low temperatures: 550-650 °C. High temperature: 750-950 °C.

The fracture surface demonstrates a typical cup and cone appearance, with plastic deformation relatively uniformly spread across the whole gauge before localized and failed toward the end of tensile tests. The microvoids seen in this sample are closely similar to the ones

found on the in-situ SEM tensile test at 750 °C (Figure 10(c)). Inevitably, in-situ SEM testing is prone to encounter larger scatters due to the complexity for setup, this is unlikely to result from material variations, rather experimental variables and the need to interruption for imaging.

Table 6. Comparision of tensile properties between in-situ SEM and standard laboratory tests.

Temperature (°C)	$\sigma_{0.2}$ (MPa)		UTS (MPa)		Elongation (%)	
	In-situ SEM	Standard	In-situ SEM	Standard	In-situ SEM	Standard
550	227	170	594	565	44	43
650	168	168	517	472	36	39
750	174	165	368	324	42	47

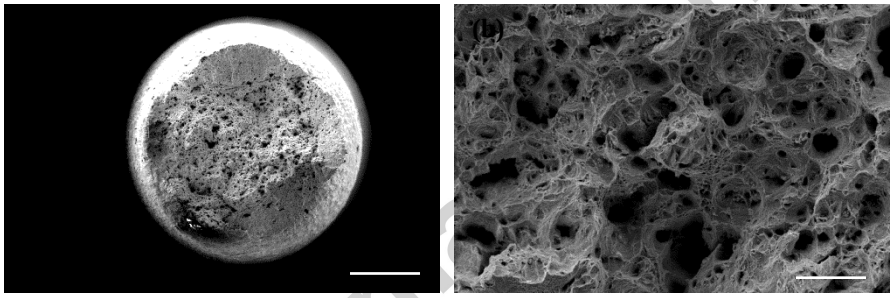

Figure 16. SEM fractographs of a cylindrical testpiece after testing at 750°C: (a) cup and cone fracture surface appearance; and (b) details of the microvoids formed in the center of the testpiece.

5. Conclusions

In-situ SEM tensile experiments were conducted to investigate tensile properties and deformation mechanisms of the Alloy 709 in a temperature range of room temperature to 950°C. Following conclusions can be drawn:

- Alloy 709 shows typical stress-strain curves of austenite stainless steels with an excellent work hardening capability up to a temperature of 650°C and a superb ductility at all temperatures.

- Serrated stress strain curves were observed at 550, 650 and 750 °C under the faster strain rate applied. At the 2.61×10^{-4} /min strain rate, serrated plastic deformation was observed to extended to 800 °C.
- The deformation mechanism was slip dominated up to 650 °C. At high temperatures, creep mechanisms are observed in the sample in the form of intergranular void formation and micro crack growth. With increase in temperature, the slip activation is observed at higher strains, with void nucleation and coalescence observed at lower strains.
- Samples tested at all temperatures failed via transgranular crack propagation, even though crack initiation was intergranular in nature. Orientation of the sample did not affect the deformation mechanism.
- Phase transformation was observed in the samples tested at high temperatures. At 650 °C, ferrite content (primarily at the grain boundaries) in the sample increased with increased exposure to the temperature during loading. The ferrite content was significantly larger at 950 °C. This could accelerate the creep cavitation at the ferrite-austenite interface.

6. Acknowledgement

This study is part of a project funded by the Department of Energy, DOE-NEUP RC-3.2, Creep and Creep-Fatigue Crack Growth Mechanisms in Alloy 709, award: 2015-1877/DE-NE0008451. The authors would also like to thank Hitachi High Technologies America for ion-milling the samples.

7. References

[1] Thomas Sourmail, Precipitation in creep resistant austenitic stainless steels, Mater. Sci. Technol. 17 (2001) 1–14.

[2] Y. Minami, H. Kimura, Y. Ihara, Microstructural changes in austenitic stainless steels during long-term aging, Mater. Sci. Technol. 2 (1986) 795–806.

[3] P.J. Maziasz, R.W. Swindeman, Development of creep resistant austenitic stainless steels for advanced steam cycle superheater application, LEGIBILITY Not. (1987) 619.

[4] M.C. Carroll, L.J. Carroll, Fatigue and creep–fatigue deformation of an ultra-fine precipitate strengthened advanced austenitic alloy, Mater. Sci. Eng. A. 556 (2012) 864–877. doi:10.1016/j.msea.2012.07.082.

[5] Y. Yamamoto, M.P. Brady, Z.P. Lu, C.T. Liu, M. Takeyama, P.J. Maziasz, B.A. Pint, Alμmina-Forming Austenitic Stainless Steels Strengthened by Laves Phase and MC Carbide Precipitates, Metall. Mater. Trans. A. 38 (2007) 2737–2746. doi:10.1007/s11661-007-9319-y.

[6] M.P. Brady, Y. Yamamoto, M.L. Santella, L.R. Walker, Composition, Microstructure, and Water Vapor Effects on Internal/External Oxidation of Alμmina-Forming Austenitic Stainless Steels, Oxid. Met. 72 (2009) 311–333. doi:10.1007/s11085-009-9161-2.

[7] Y. Yamamoto, M.P. Brady, Z.P. Lu, P.J. Maziasz, C.T. Liu, B.A. Pint, K.L. More, H.M. Meyer, E.A. Payzant, Creep-resistant, Al2O3-forming austenitic stainless steels, Science. 316 (2007) 433–436.

[8] S. Sham, ARC Materials Development - Accomplishments and Plans, (n.d.). https://www.energy.gov/sites/prod/files/2013/09/f2/ARC-Matls-CrossCut-2013.pdf.

[9] T. Sourmail, H. Bhadeshia, Microstructural evolution in two variants of NF709 at 1023 and 1073 K, Metall. Mater. Trans. A. 36 (2005) 23–34.

[10] J.-H. Shim, E. Kozeschnik, W.-S. Jung, S.-C. Lee, D.-I. Kim, J.-Y. Suh, Y.-S. Lee, Y.W. Cho, Nμmerical simulation of long-term precipitate evolution in austenitic heat-resistant steels, Calphad. 34 (2010) 105–112. doi:10.1016/j.calphad.2010.01.001.

[11] P. Rodriguez, Serrated plastic flow, Bull. Mater. Sci. 6 (1984) 653–663.

[12] K.G. Samuel, S.L. Mannan, P. Rodriguez, Serrated yielding in AISI 316 stainless steel, Acta Metall. 36 (1988) 2323–2327.

[13] K. Peng, K. Qian, W. Chen, Effect of dynamic strain aging on high temperature properties of austenitic stainless steel, Mater. Sci. Eng. A. 379 (2004) 372–377. doi:10.1016/j.msea.2004.03.004.

[14] B.K. Choudhary, Activation energy for serrated flow in type 316L(N) austenitic stainless steel, Mater. Sci. Eng. A. 603 (2014) 160–168. doi:10.1016/j.msea.2014.02.083.

[15] B.K. Choudhary, Influence of Strain Rate and Temperature on Tensile Deformation and Fracture Behavior of Type 316L(N) Austenitic Stainless Steel, Metall. Mater. Trans. A. 45 (2014) 302–316. doi:10.1007/s11661-013-1978-2.

[16] Z.Q. Xu, Y.Z. Shen, Serrated Flow in 316LN Austenitic Stainless Steel, Appl. Mech. Mater. 455 (2013) 159–162. doi:10.4028/www.scientific.net/AMM.455.159.

[17] D.W. Kim, W.-S. Ryu, J.H. Hong, S.-K. Choi, Effect of nitrogen on the dynamica strain agening behavioir of typr 316L stainless steel., J. Mater. Sci. 33 (1998) 675–679. doi:https://doi.org/10.1023/A:1004381510474.

[18] S. Hong, The tensile and low-cycle fatigue behavior of cold worked 316L stainless steel: influence of dynamic strain aging, Int. J. Fatigue. 26 (2004) 899–910. doi:10.1016/j.ijfatigue.2003.12.002.

[19] G. T.W, K. W., T. C.L., Development of a Resistance Heating Facility for the Determination of Tensile Properties of Aircraft and Missile Alloys., Avco Corporation, 1963. https://icme.hpc.msstate.edu/mediawiki/index.php/File:B2.PNG (accessed October 25, 2017).

[20] A.D. Warren, I.J. Griffiths, R.L. Harniman, P.E.J. Flewitt, T.B. Scott, The role of ferrite in Type 316H austenitic stainless steels on the susceptibility to creep cavitation, Mater. Sci. Eng. A. 635 (2015) 59–69. doi:10.1016/j.msea.2015.03.048.